



Highly active Fe₂O₃-doped TiO₂ photocatalyst for degradation of trichloroethylene in air under UV and visible light irradiation: Experimental and computational studies

Alireza Banisharif^a, Abbas Ali Khodadadi^{a,*}, Yadollah Mortazavi^a, Azam Anaraki Firooz^b, Javad Beheshtian^b, Shaghayegh Agah^a, Sadra Menbari^a

^a Catalysis and Nanostructured Materials Laboratory, School of Chemical Engineering, College of Engineering, University of Tehran, Enghelab Ave., P.O. Box 11365-4563, Tehran, Iran

^b Department of Chemistry, Faculty of science, Shahid Rajaee Teacher Training University, P.O. Box 16785-163, Lavizan, Tehran, Iran

ARTICLE INFO

Article history:

Received 1 July 2014

Received in revised form

26 September 2014

Accepted 8 October 2014

Available online 18 October 2014

Keywords:

Trichloroethylene

Titanium

Iron

Photocatalyst

DFT

ABSTRACT

0.0–5.0 wt% Fe₂O₃-doped TiO₂ photocatalysts were synthesized by an ultrasonic-assisted co-precipitation method and used for degradation of 500 ppm trichloroethylene (TCE) in air. The photocatalysts were treated at 100–400 °C and characterized by high resolution transmission electron microscopy (HRTEM), powder X-ray diffraction (XRD), BET surface area, and Raman, UV–vis, and photoluminescence (PL) spectroscopies. For the samples treated at 100 °C, XRD patterns show no significant peaks, while HRTEM micrographs indicate crystalline structures and diffraction patterns and Raman spectra reveal wide and weak peaks of anatase TiO₂. As 0.1 wt% Fe₂O₃ is added to TiO₂, the surface area increases by a factor of 1.87 and reach to 448 m²/g. UV–vis analyses indicate that, as the Fe₂O₃ content of the samples increases, the band gap energies decrease from 3.22 eV for the pure TiO₂ to 2.60 eV for 5.0 wt% Fe₂O₃-doped TiO₂. Density functional theory simulations show that, when Fe³⁺ is doped into or FeO, Fe₂O₃ or Fe₄O₆ is adsorbed on anatase TiO₂, the band gap reduces and the iron oxide–TiO₂ show photocatalytic activity in visible light region. The synthesized TiO₂ showed about two times higher photocatalytic activity for TCE removal than that of Degussa P25. Moreover, 0.1 wt% Fe₂O₃-doped TiO₂ sample dried at 100 °C showed a maximum photocatalytic TCE conversion of about 97% with minor amounts of CO as a hazardous byproduct. As the treatment temperature of the samples increase, the photocatalytic activity declines. Significant photocatalytic degradation of TCE was also observed for the Fe₂O₃-doped TiO₂ samples, under visible light irradiation.

© 2014 Elsevier B.V. All rights reserved.

1. Introduction

During the last decades, photocatalytic degradation of volatile organic compounds (VOCs) has attracted much attention due to hazardous problems of air pollution for human beings [1,2]. Among the VOCs, chlorinated volatile organic compounds (CVOs) such as trichloroethylene (TCE) have been widely used as solvents in industrial processes and for cleaning purposes. Different chemical and physical processes, such as incineration, adsorption, absorption, condensation, bio-filtration, and heterogeneous catalytic and photocatalytic oxidation methods have been employed to remove TCE [3–5]. Combinations of heterogeneous photocatalytic semiconductors with ultraviolet (UV) irradiation are very effective in

treating chlorinated aliphatic gases such as TCE. More recent studies are focused on photocatalytic oxidation of TCE in liquid rather than in gas-phase, using semiconductors [6–16]. Among the semiconductors, TiO₂ photocatalyst has been used for purifying air, due to its low cost, excellent stability, and high photocatalytic activity [6–14].

Separation of electrons and holes as well as oxygen vacancies and defects created by metal dopants enhance the efficiency of the semiconductor photocatalysts [15]. There are a few reports about the effect of metal-doped TiO₂ on photocatalytic degradation of TCE in air. For instance, Driessen and Grassian [16] have investigated the gas-phase photooxidation of trichloroethylene (TCE) on Pt/TiO₂. They found that Pt particles enhance the photooxidation of TCE at longer wavelengths. Park et al. [17] have also shown that the photocatalytic activities of Mo-, Nb- and W-doped TiO₂ thin films significantly improved TCE degradation. It has been proposed that the high valence cation-doped TiO₂ are beneficial in the

* Corresponding author. Tel.: +98 2166967792; fax: +98 2166967793.
E-mail address: Khodadadi@ut.ac.ir (A.A. Khodadadi).

transfer and separation of photo-generated electrons and holes in the TiO_2 bulk and on the surface. Tanimura et al. [18] have investigated the effect of addition of some cations like Cr, Fe, Ni, Cu and Pt, or Cato TiO_2 for degradation of TCE. Sun et al. [19] prepared highly efficient Pt/N- TiO_2 photocatalyst to facilitate the degradation of volatile organic compounds (VOCs) under $\lambda > 490 \text{ nm}$. Ou et al. [20] have also investigated the effect of Pt and Pd on the TCE photocatalytic degradation and concluded that especially Pd had a significant negative effect on TCE degradation.

Almost all previous photocatalytic studies on TiO_2 were focused on the use of its crystalline forms. It is suggested that amorphous TiO_2 contains high concentrations of defects with rapid electron-hole pair recombination that suppresses the photocatalytic activity [21]. However, amorphous TiO_2 with higher surface area may show high adsorption capacity because of high concentration of hydroxyl groups on their surface and may show higher photocatalytic activity than the crystalline phases [22–26].

Recently, theoretical calculations on Fe-doped TiO_2 have been performed, using the density functional theory (DFT), and the interaction between the valence electrons and ionic core has been described by different functional methods such as Perdew–Burke–Eznerhof (GGA-PBE) [27,33], GGA-FP-LAPW [28], Perdew–Wang91 (GGA-PW91) [29,30], B3LYP [31,36] and Hubbard U (GGA+U) [32,34,35].

Thimsen et al. [27] have reported that the predicted band gap of Fe-doped TiO_2 is 0.9 eV lower than that of TiO_2 , while 0.69 eV is reported in another study [28]. Yu et al. [30] have simulated Fe doping effects using $(\text{Fe}_x\text{Ti}_{1-x})\text{O}_2$ anatase supercell and reported that the DFT calculation further confirmed the red shift of absorption edges and the narrowing of the band gap of Fe- TiO_2 nanorods. Yalcin et al. [31] have proposed models for undoped and Fe^{3+} -doped anatase TiO_2 clusters and indicated that the visible light activity in Fe^{3+} -doped TiO_2 is due to the introduction of additional electronic states within the band gap. Nolan [32] have presented first principles simulations of iron oxide clusters adsorbed at the rutile TiO_2 (110) surface to elucidate the origin of the visible light photocatalytic activity of iron oxide modified TiO_2 . Wellia et al. [33] have proposed iron doped- TiO_2 model by placing one Fe atom in

the lattice of TiO_2 crystal and studied the structural and electronic properties, using DFT. Nolan et al. [34] have calculated surface-modified TiO_2 using DFT to describe Fe and Ti oxidation states consistently.

In this work, we synthesized 0.0–5.0 wt% Fe_2O_3 -doped TiO_2 nanoparticles by ultrasonic-assisted co-precipitation method, treated them at various temperatures, and used them for photocatalytic degradation of TCE in dry and humid air, under UV and visible light irradiation. In addition, we used density functional theory (DFT) calculations to describe the effect of Fe_2O_3 on the electronic structure of anatase TiO_2 .

2. Experimental

2.1. Preparation of Fe_2O_3 -doped TiO_2

All chemicals were analytic grade from Merck and used without further purification and treatment. The ultrasonic assisted co-precipitation method was employed to prepare Fe_2O_3 -doped TiO_2 nanoparticles. Titanium tetrachloride (TiCl_4) and ferric nitrate ($\text{Fe}(\text{NO}_3)_3 \cdot 9\text{H}_2\text{O}$) were used as precursors for Fe_2O_3 -doped TiO_2 powders preparation. A solution of NH_4OH (0.1 M) was added drop-wise to 125 ml of 0.5 M TiCl_4 under ultrasonication at 80°C with constant stirring for about 2 h, to increase the pH to 9. The TiO_2 nanoparticles were collected and washed several times by distilled water. For the 1.0 wt% Fe_2O_3 -doped TiO_2 sample as an example, the TiO_2 nanoparticles suspension at pH 7 was introduced into the solution containing 0.55 g of Na_2CO_3 dissolved in 200 ml deionized water under ultrasonication at 80°C . The 0.25 g of $\text{Fe}(\text{NO}_3)_3 \cdot 9\text{H}_2\text{O}$ was dissolved in deionized water and then added to the solution drop-wise under ultrasonication and stirring for about 2 h. Finally, the 1.0 wt% Fe_2O_3 -doped TiO_2 nanoparticles were collected and washed several times by distilled water and dried in an oven at 100°C for 12 h. Similarly, we also synthesized Fe_2O_3 -doped TiO_2 nanoparticles with other ratios. Fe_2O_3 -doped TiO_2 samples with 0.00, 0.05, 0.1, 0.2, 0.5, 1.0, 2.0, 5.0 wt% of Fe_2O_3 to TiO_2 are denoted as T, FT0.05, FT0.1, FT0.2, FT0.5, FT1, FT2 and FT5, respectively.

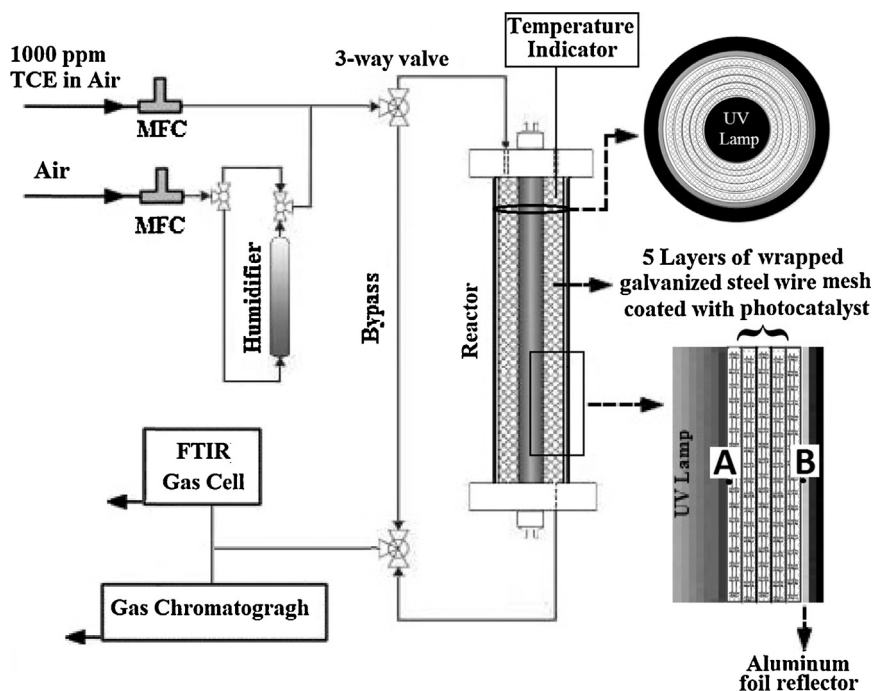


Fig. 1. Schematic of the experimental setup used for photocatalytic oxidation of TCE in air.

Also Degussa P-25 TiO₂ was used as a commercial sample for comparison.

The 0.1 wt%-Fe₂O₃-doped TiO₂ sample was dried at 100 °C and calcined at 200 °C, 300 °C and 400 °C for 2 h at a rate of 4 °C/min and are denoted as FT0.1–100, FT0.1–200, FT0.1–300 and FT0.1–400, respectively.

2.2. Coating of the photocatalysts on galvanized steel wire mesh substrates

Galvanized steel wire mesh (Tyler series number 14) was used as substrates for the photocatalyst deposition. A 22 × 34 cm wire mesh was first wrapped into a 5-layers cylinder of 2.5 cm OD and 22 cm height, with a 1.6 cm hole in the center for placing the UV-lamp with the same diameter (see Fig. 1). Prior to coating, the wrapped wire mesh photocatalyst substrate was washed with acetone and distilled water. The coating was formed on the wire mesh substrate by a dip-coating method. The wire mesh substrate was dipped for 10 min into aqueous slurry containing 10 wt% photocatalyst powder of about 0.1 μm average size measured by dynamic light scattering (DLS, Micromeritics, NanoPlus-1, Fig. S1). 0.5 and 1.0 g loadings of the photocatalysts on the wire mesh substrates with about 3 and 6 μm thicknesses were prepared by 3 and 6 times dip coating, respectively (Fig. S2). The coated mesh was dried in an oven at 100 °C for 30 min and calcined at various temperatures.

2.3. Characterization

Dynamic light scattering (Micromeritics, NanoPlus-1) was used to obtain the particle size distribution of the photocatalyst particles suspended in the dip-coating slurry. Optical microscope (Radical RMM-7T) was used to study the uniformity of the photocatalyst coatings on the wire mesh substrates.

XRD patterns of the photocatalysts were recorded using a Philips, Holland Xpert X-ray powder diffraction (XRD) with CuK_α (λ = 1.5406 Å) radiation. Average crystallite sizes of the samples were estimated using Scherrer's formula: $D = 0.9\lambda / \beta \cos\theta$ [2], where D is diameter of the nanoparticles, λ (CuK_α) = 0.15406 nm and β is the full-width at half-maximum of the diffraction lines. The specific surface areas of the samples were measured by Brunauer–Emmet–Teller (BET) method, using a CHEMBET-3000 apparatus and the approximate average particle diameter from BET specific surface area was calculated from $d_{\text{BET}} = 6000 / (\rho \times S_{\text{BET}})$, where S_{BET} is BET surface area (m²/g) and ρ is the skeletal density (g/cm³). For a rough estimate of sizes, the nanoparticles are assumed to have spherical shape [5].

The band gaps of TiO₂ samples were determined by UV–vis spectrophotometer (PG T80/T80⁺). The spectra were recorded at room temperature in the wavelength range of 200–800 nm with 0.5 nm accuracy. The photoluminescence (PL) spectra of the photocatalyst samples were recorded by applying a photoluminescence spectrophotometer (Avantes/Avaspec 2048) at room temperature in the wavelength range of 400–800 nm with the measurement accuracy of 0.04–20 nm. The Raman spectra were obtained at room temperature using a SENTERRA Raman spectrometer (Bruker, Germany) equipped with CCD detector in the wavelength range of 100–3500 cm^{−1}. These laser diodes emit both visible and invisible laser radiation in the near infrared region laser of 785 nm. The morphology of the samples was shown by using a high resolution transmission electron microscopy (HRTEM; Philips CM200, 200 kV) as well as selected area electron diffraction in the bright field. Also, energy dispersive X-ray (EDX-700 Shimadzu) was used for elemental analysis of the photocatalysts.

2.4. Photocatalytic degradation of trichloroethylene

The activity of the photocatalyst samples coated on wire meshes for degradation of trichloroethylene (TCE), as a model compound for unsaturated chlorinated VOCs, in air was studied using a reaction system shown in Fig. 1. 1000 ppm TCE in zero air (99.99%, Roham Gas Co.) with a flow rate of 250 sccm controlled by the mass flow controllers (Unit 8100), were mixed with zero air to obtain 500 ppm TCE in air, as the feed for the photocatalytic reaction system. All photocatalytic activity measurements were performed at 40 °C and atmospheric pressure. The feed and the photocatalytic reactor effluent gases at various times on stream up to 60 min were analyzed by an on-line Carle 400-A gas chromatograph (GC) equipped with an FID and a column packed with Carbowax 20 M at 110 °C. CO and CO₂ after separation were converted to methane in a methanizer with a Ru/Al₂O₃ catalyst at 420 °C. An online Burkert Fourier transform infrared spectroscopy (FTIR) instrument was used to identify the effluent gases from the photooxidation of TCE. Conversion of TCE is given by:

$$\text{Conversion (\%)} = \frac{C_0 - C}{C_0} \times 100 \quad (1)$$

where, C_0 is the inlet concentration of TCE and C is the concentration of TCE in the effluent gas. The conversion of TCE on the photocatalysts was measured after observing the steady state value under UV irradiation, after 60 min time on stream TOS). Also, a blank test was carried out on the bare wire mesh substrate, without the photocatalyst coating, for comparison. To study the effect of water vapor in some of the experiments, the zero air was humidified by passing it through a bubbler containing DI water at room temperature, to obtain about 50% relative humidity (RH) of the feed to the reaction system.

The annular reactor was equipped with a UV lamp and the photocatalyst-coated wire mesh. An aluminum foil was wrapped on the wire mesh external surface, to reflect the UV radiation into the reactor. Dimensions of the annular reactor were 25 mm OD, 16 mm ID and 25 cm in height. The effective volume of the photocatalytic reactor was 67 cm³ (Fig. S3).

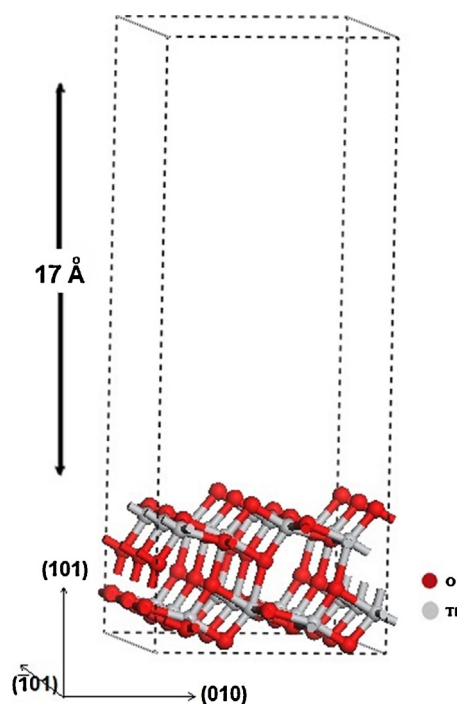


Fig. 2. TiO₂ vacuum slab.

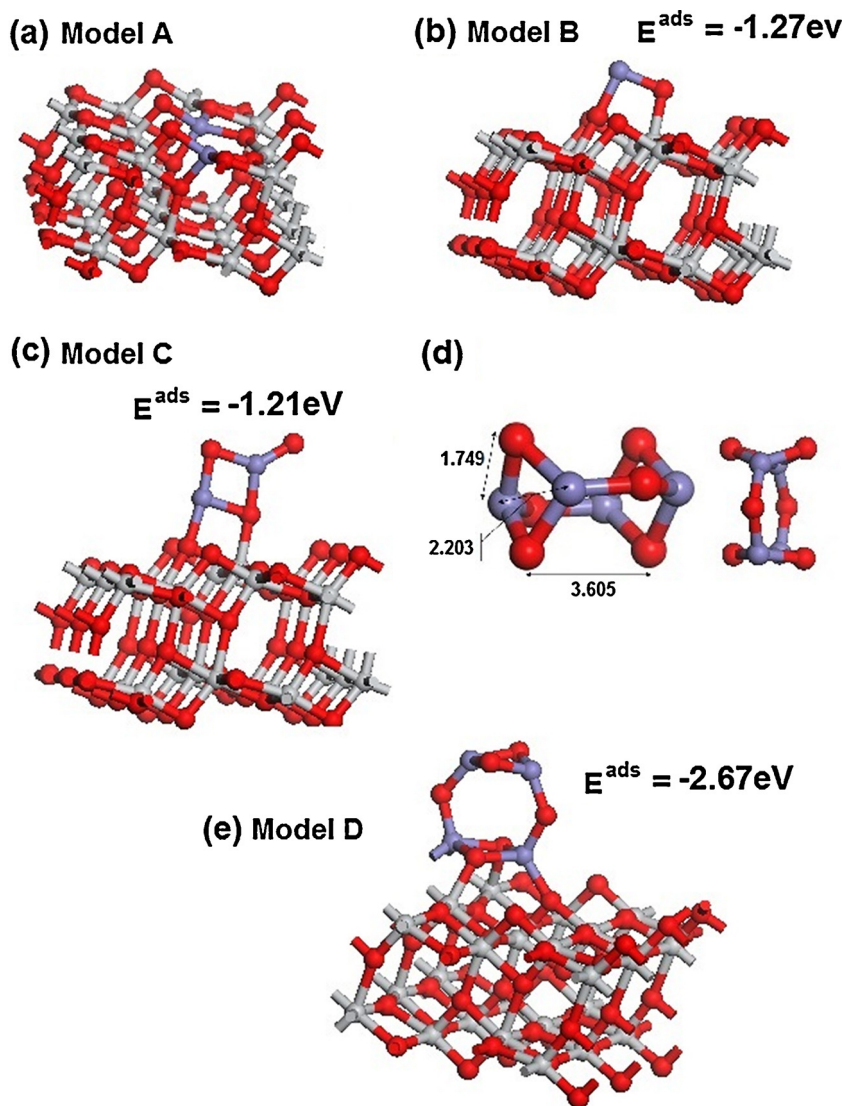


Fig. 3. Optimized structures of (a) Fe^{3+} doped TiO_2 (Model A), (b) FeO adsorbed on the anatase (101) surface (Model B), (c) Fe_2O_3 adsorbed on the anatase (101) surface (Model C), (d) the structure of Fe_4O_6 cluster, (e) Fe_4O_6 cluster adsorbed on the anatase (101) surface (Model D) (gray for titanium; red for oxygen; and blue for Fe^{3+}). (For interpretation of the references to color in this figure legend, the reader is referred to the web version of this article.)

The UV radiation was supplied by a germicidal white light lamp (8W, Philips, Holland). The wavelength range of this lamp was 200–300 nm with a maximum light intensity at 254 nm. The intensity of the UV lamp measured by the UV radiometer (VLX-3W, Cole-Parmer) in A and B positions were 27 and 8 W/m^2 , respectively (Fig. 1). Fluorescent black lamp (8W, Philips, Holland) with wavelengths in the range of 350–400 nm and maximum intensity at 365 nm and three visible light lamps of blue, green and red colors with the same power of 8 W were also used as other light sources.

2.5. Computational method

Anatase TiO_2 has a tetragonal structure with bulk crystal parameters of $a = 3.76 \text{ \AA}$ and $c = 9.48 \text{ \AA}$, which are consistent with the experimental data. We considered a 3×1 anatase (101) surface supercell, corresponding to 24 $[\text{TiO}_2]$ units of anatase in XY-plane and perpendicular to Z-axis of the supercell. A TiO_2 slab with an imposed vacuum space of about 17 \AA separation was considered to allow surface reactions to occur and to ensure no interaction with the lowest layer of the upper slab in the direction

perpendicular to the Z-axis of the super cell [27–36]. Fig. 2 shows that, in anatase TiO_2 , each Ti atom is bonded to its four nearest and two second nearest oxygen neighbors. Fig. 3 presents four proposed models for the iron oxide–anatase TiO_2 . In Model A, the structure of the iron oxide–anatase TiO_2 was constructed by replacing two Ti^{4+} with two Fe^{3+} cations. This induces a charge imbalance, resulting in the formation of an oxygen vacancy [35]. Models B, C and D were constructed by adsorption of FeO , Fe_2O_3 and Fe_4O_6 clusters on the anatase (101) surface, respectively. Such small and molecular sized metal oxide clusters are good models of the dispersed and molecular scale adsorbed species described by Tada et al. and Nolan et al. [32,34,73].

The full geometry optimizations and property calculations were performed with the quantum-ESPRESSO suite of codes, in which the DFT methodology is implemented using plane waves expansions and pseudopotentials [30–36]. The widely used generalized gradient approximation (GGA) with the exchange–correlation functional parameterized by Perdew and Wang (PW91) was adopted, using spin-polarized calculations. We used a plane wave basis set with an orbital cutoff distance of 3.5 \AA [29,30]. We explicitly include the 3s and 3p semicore states of Ti in our calculations. The

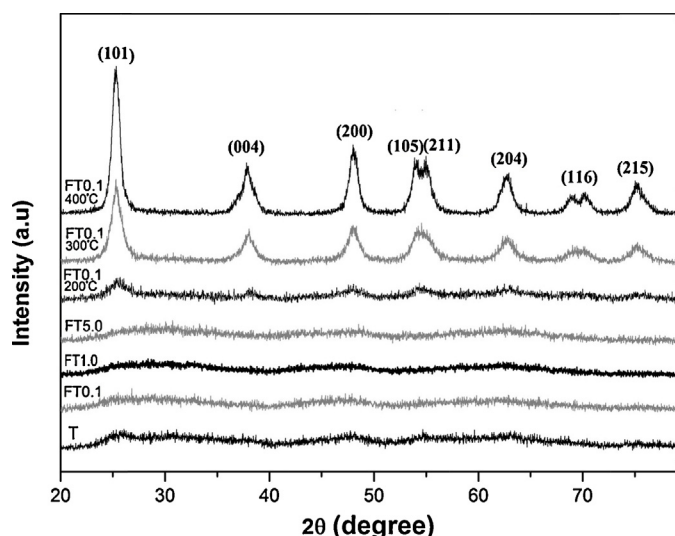


Fig. 4. X-ray diffraction patterns of dried TiO_2 and the ones doped with various amounts of Fe_2O_3 and 0.1 wt% $\text{Fe}_2\text{O}_3\text{-TiO}_2$ sample calcined at 200 °C, 300 °C and 400 °C for 2 h.

electronic wave functions are expanded in plane waves basis set with a kinetic energy cutoff of 200 Ry. The Brillouin zone was sampled with $1 \times 2 \times 2$ Monkhorst-Pack k-points [36] mesh, to ensure convergence.

The undoped TiO_2 surface, the Fe^{3+} doped in TiO_2 lattice, the iron oxide clusters adsorbed on TiO_2 surface and the free Fe_2O_3 and Fe_4O_6 clusters are calculated in the same periodic supercell, with the same plane wave cutoff energy, the same k-point sampling grid, the same DFT approach and the same PAW potentials, ensuring consistency between calculations. To study cluster adsorption, the clusters are positioned in a number of configurations at the (1 0 1) surface and then a full relaxation is performed within a fixed supercell. The adsorption energy is computed from $(2)E^{\text{ads}} = E(\text{iron oxide-TiO}_2) - \{E(\text{iron oxide}) + E(\text{TiO}_2)\}$ where $E(\text{iron oxide-TiO}_2)$ is the total energy of the iron oxide adsorbed on the surface, and $E(\text{iron oxide})$ and $E(\text{TiO}_2)$ are the total energies of the free iron oxide and the bare surface, respectively; a negative adsorption energy signifies that iron oxide adsorption is stable.

3. Result and discussion

3.1. Characterization of photocatalysts

The XRD patterns of the Fe_2O_3 -doped TiO_2 samples with different proportions of Fe_2O_3 dried at 100 °C and the FT0.1 annealed at various temperatures are presented in Fig. 4. Flat base lines with very weak bumps in XRD patterns of all the dried samples indicate the amorphous phase of the samples. Due possibly to amorphous phase, too small crystallites, and/or doping of iron ions into TiO_2 matrix, no XRD diffraction patterns of the dopants could be detected [26,37–40]. By calcinations of FT0.1 samples at higher temperatures up to 400 °C, the structure of crystalline anatase TiO_2 was evolved. Diffraction peaks of anatase phase TiO_2 (JCPDS file no. 21-1272) at 25.25°, 37.8°, 47.9°, 53.6°, 55.8° and 62.4° two-theta can be attributed to (1 0 1), (0 0 4), (2 0 0), (1 0 5), (2 1 1) and (2 0 4) crystal planes of anatase structure of the TiO_2 , respectively (Fig. 4). Due to low amount of 0.1 wt% Fe_2O_3 , its amorphous phase and/or too small crystallites, no peak belongs to Fe_2O_3 , even after calcination at 400 °C. As the annealing temperature increases, the full width at half maximum (FWHM) of the TiO_2 peaks reduce and their intensities increase. Therefore, the TiO_2 crystallites growth is augmented

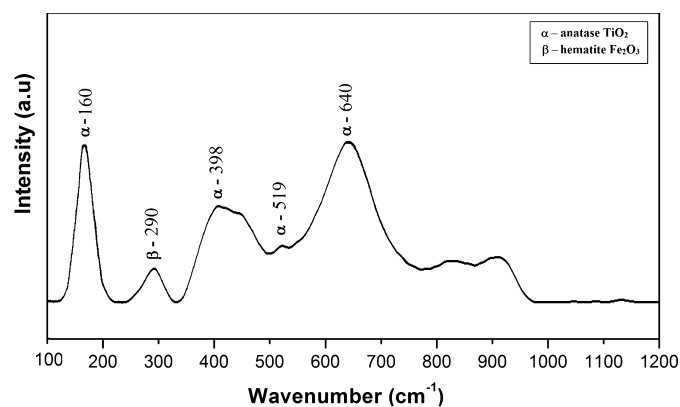


Fig. 5. Raman spectrum of 0.1% $\text{Fe}_2\text{O}_3\text{-TiO}_2$.

at higher temperatures [41]. The crystallite sizes of the samples estimated by the Scherrer's formula are presented in Table 1.

Raman spectrum of FT0.1 sample dried at 100 °C is shown in Fig. 5. Raman peaks of the sample are attributed to anatase phase of TiO_2 and hematite Fe_2O_3 . Due to the low concentration of Fe and its distribution in TiO_2 , the bands related to iron oxides are not observed. One band corresponding to Fe–O–Ti bond is observed at approximately 300 cm^{-1} , indicating that Fe^{3+} replaces some Ti^{4+} in the lattice sites of the crystalline structure of Fe– TiO_2 samples [42]. Moreover, the strongest mode of anatase TiO_2 at 144 cm^{-1} is shifted to 160 cm^{-1} , the full width at half maximum (FWHM) is broader and the mode intensity is smaller. This can be attributed to the effect of smaller particle size and/or the Fe ions impurities substitute for the Ti sites in the anatase TiO_2 phase, and thus affects the force constant and vibrational amplitudes of the nearest neighbor bond [43–48].

HRTEM analysis was used to further examine morphology, particle size, and crystallinity of the samples. HRTEM micrographs of FT0.1 sample dried at 100 °C reveal the formation of small TiO_2 amorphous and anatase crystals mostly in the range of 2–8 nm (Fig. 6a and b and insets). The average particle size of 3.2 nm for FT0.1 sample estimated from BET surface area measurement (Table 1) is in good agreement with the HRTEM results. The amorphous and crystalline phase of $\text{Fe}_2\text{O}_3\text{-TiO}_2$ in the FT0.1 sample can also be observed by phase-contrast image in Fig. 6c. The HRTEM results are not incomparable with XRD ones, since the XRD technique provides clear information only on sufficiently large crystals, but no diffraction pattern is observed for too small and/or amorphous particles [49]. Fig. 6b and c inset and present crystal lattice planes with the lattice fringes of 0.35 and 0.23 nm corresponding to the (1 0 1) and (0 1 1) crystal planes of anatase TiO_2 , respectively [39,50]. The fringe spacing of 0.23 nm also matches with the d-spacing of the (0 0 6) crystal planes of the $\alpha\text{-Fe}_2\text{O}_3$ [51]. Due to similar ionic radii, Fe^{3+} can substitute with Ti^{4+} in a mixed oxide system [52]. At low concentrations, iron cations are fully dispersed into the TiO_2 matrix by formation of solid solutions with titanium oxide. However, the solubility limit of Fe ions in TiO_2 , may lead to the formation of $\alpha\text{-Fe}_2\text{O}_3$. It is shown that iron ions decrease the crystallization rate of TiO_2 , leading to small particles [52]. Furthermore, the interface of the sample is tilted and not coherent. The black arrows (Fig. 6c) show a distorted and concentrated defect area along the interface.

Based on the HRTEM results, we proposed four models of Fe doped into TiO_2 lattice (Model A) and FeO (Model B), Fe_2O_3 (Model C) and Fe_4O_6 cluster (Model D) adsorbed on anatase TiO_2 (1 0 1), for DFT calculations of electronic structure of iron oxide– TiO_2 . In Model A, all Fe–O bond lengths are shorter than those of Ti–O. This indicates that, as Ti^{4+} is replaced by Fe^{3+} cations, the overall

Table 1

Photocatalyst samples BET surface areas, average particle sizes, crystallite sizes, band gap energies, and TCE conversions on 0.5 and 1.0 g photocatalysts.

Sample name	BET surface area (m ² /g)	Average particle size (nm)	Crystallite size (d _{XRD} , nm)	Band edge (nm)	Band gap (eV)	TCE conversion (%) on 1.0 g photocatalyst	TCE conversion (%) on 0.5 g photocatalyst
P-25	50	28.4	–	400	3.10	0.34	0.20
TiO ₂	240	5.9	–	385	3.22	0.63	0.40
FT0.05	379	3.7	–	402	3.08	0.92	0.73
FT0.1	448	3.2	–	410	3.02	0.97	0.85
FT0.2	398	3.6	–	422	2.94	0.90	0.69
FT0.5	242	5.9	–	430	2.88	0.70	0.44
FT1	190	7.5	–	452	2.74	0.50	–
FT2	205	6.9	–	462	2.68	0.54	–
FT5	230	5.7	–	476	2.60	0.28	–
FT0.1–200	397	3.6	3.5	412	3.01	–	0.79
FT0.1–300	213	6.7	6.4	415	2.99	–	0.75
FT0.1–400	140	10.1	9.17	418	2.97	–	0.54

volume reduces, due to the difference in the radii of the ions: 64 pm for Fe³⁺ and 68 pm for Ti⁴⁺ [31]. In either B or C Model, there is just one stable structure of FeO and Fe₂O₃ adsorbed on anatase TiO₂ (1 0 1), respectively. In Model B, the formed Ti–O and Fe–O distances are 1.94 and 1.81 Å, respectively. In Model C, the formed Ti–O and Fe–O distances are 2.01 and 1.84 Å, respectively.

As shown in Fig. 3d, for Fe₄O₆ cluster, all Fe–Fe pairs are bridged by one O atom with Fe–O–Fe angles close to 90. The distances between Fe–O, Fe–Fe and O–O are about 1.75, 2.2 and 3.60 Å, respectively. As shown in Model D, this cluster was adsorbed strongly at the anatase (1 0 1) surface with two oxygen atoms and one iron atom. The formed Ti–O and Fe–O distances are 2.01 and 1.93 Å, respectively.

All adsorption energies of iron oxides adsorbed on TiO₂, relative to free iron oxides and TiO₂, are also calculated and shown in Fig. 3. The negative adsorption energies signify that the iron oxides adsorbed on TiO₂ surface are stable.

The energy-dispersive X-ray (EDX) spectrum of the FT0.1 in Fig. 6d shows the presence of Ti and Fe in the FT0.1 and the signal of Cu is from the copper net. A selected area electron diffraction (SAD) pattern of FT0.1 is presented in Fig. 6e. It shows the formation of TiO₂ anatase phase. However, the brightness and intensity of polymorphic circles are weak, therefore TiO₂ is not completely and regularly crystallized. The SAD pattern of FT0.1 shows the formation of hematite Fe₂O₃ too (Fig. 6f).

The BET surface area and average particle size of the samples are shown in Table 1. The results reveal that both the quantity of Fe₂O₃ dopant and drying/calcination temperature strongly affect the specific surface area of the samples. The doping of iron-ion within suitable concentration range may lead to the larger surface areas [53–57]. The TiO₂ sample prepared by the ultrasonic-assisted co-precipitation method presents 240 m²/g surface area, 4.8 times higher than that of P25. FT0.1–100 shows the highest surface area of 448 m²/g, about 9 times higher than that of P25. The doping may prevent particle agglomeration and form nanocrystalline powders with high surface area [55].

The samples BET surface areas dramatically decrease and the average sizes increase, as the drying/calcination temperature increases. The average particle sizes of the samples approximated from BET surface areas are in good agreement with the crystallite

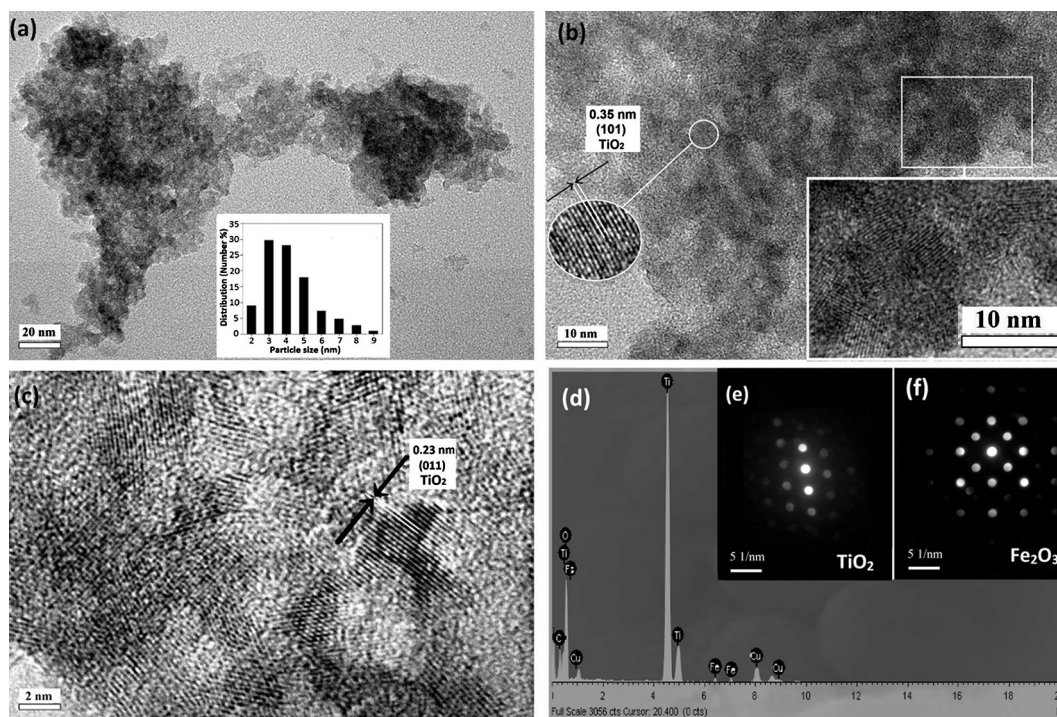


Fig. 6. HRTEM micrographs of 0.1% Fe₂O₃–TiO₂ sample (a), (b) and (c) images with increasing magnifications, (d) selected-area electron diffraction (SAD) pattern of anatase TiO₂, (e) SAD pattern of hematite Fe₂O₃, and (f) energy dispersive X-ray (EDX) pattern.

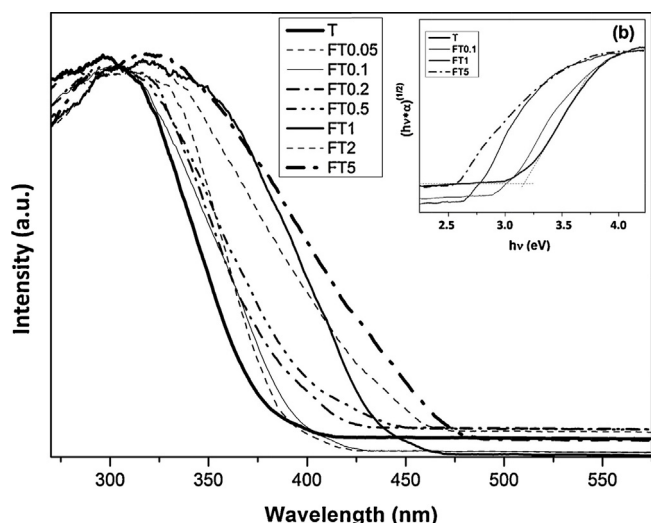


Fig. 7. UV-vis diffuse reflectance spectra of TiO_2 and 0.05–5.0 wt% Fe_2O_3 -doped TiO_2 samples, inset: the plot of Kubelka-Munk function of $[R(R_0)^{-1/2}]$ versus $h\nu$.

sizes calculated from XRD patterns of the samples annealed at 200°C and higher temperatures.

The absorption of UV-vis light by a sample is an important factor for evolution of its photocatalytic properties. It is also useful to understand absorption constant of the structural variations, resulting in band gap changes. The observed UV-vis absorption spectra of the samples are shown in Figs. 7 and 8. Summarized in Table 1, the band gaps of the samples are calculated based on the maximum absorption waves and according to Kubelka-Munk equation: $\alpha = K(h\nu - E_g)^{(1/n)}/h\nu$, where α is the absorption coefficient, E_g is the band-gap energy (eV), K is a constant, n equals 0.5 for indirect transition and 2 for the direct transition and TiO_2 is considered as an indirect semiconductor [58]. The band-gaps of Fe_2O_3 -doped TiO_2 samples (Table 1) are smaller than that of pure TiO_2 and decrease significantly with the concentration of Fe_2O_3 and slightly with drying/calcination temperature.

Band structures calculated within standard DFT underestimate the fundamental band gap of anatase TiO_2 , consistent with the earlier standard DFT results reported in the literature [31]

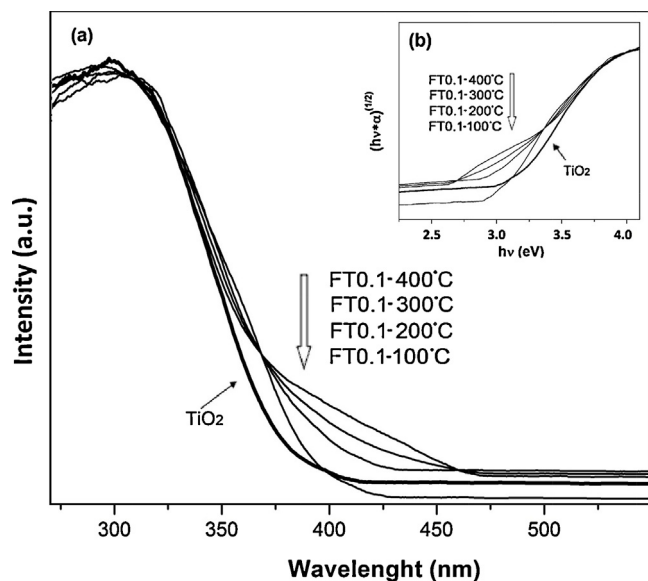


Fig. 8. The UV-vis diffuse reflectance spectra of 0.1% Fe_2O_3 -doped TiO_2 samples calcined at different temperatures, inset: the plot of Kubelka-Munk functions.

The experimental band-gap energy of about 3.22 eV for the undoped TiO_2 is adopted as the benchmark to correct the calculated values of the anatase (101) surface. The underestimated band-gap is corrected by using a scissors operator [31]. This displaces the empty and occupied bands relative to each other by a rigid shift of 0.50 eV, to bring the minimum band-gap in line with experiment. For Models A, B, C and D, the corrected band-gap energies are calculated to be 1.71, 1.60, 1.45 and 1.24 eV respectively (Fig. 9), which is consistent with other papers reports [31–36]. As shown in this figure, the zero-point energy is taken as the Fermi level.

All models energy level diagrams obtained from electronic structure calculations are displayed in Fig. 10. The band gaps energies decrease in the following order:

Undoped TiO_2 Model > Model A > Model B > Model C > Model D

The band-gaps of all models are smaller than that of the undoped TiO_2 by about 1.51–1.98 eV. In addition, as the cluster sizes in Models B–D increase, the band gap energies reduce (Fig. 10). In contrast, in Model A with two iron atoms, the formation of an oxygen vacancy causes a slight increase in the band-gap energy [35]. In the doping process (Model A), the Fe^{3+} cation replaces Ti^{4+} and Fe^{3+} will act as an electron donor and form donor level close to the conduction band of TiO_2 , resulting in a smaller energy transition [59]. The DFT calculation results give a good explanation for experimental optical absorption (Fig. 7) in a smaller energy transition, which leads to the visible light photoactivation.

Also Fig. 10 shows that the bottom of the conduction bands has decreased by about 0.32, 0.23 and 0.22 eV for Models A, C and D, respectively, while that of Model B has increased by about 0.17 eV, as compared to undoped TiO_2 . In addition, the top of the valence bands has increased in the range of 1.24–1.99 eV, depending on the model.

FT5 sample containing 5.0 wt% Fe_2O_3 shows the highest red-shift of the band ($E_g = 2.60$ eV), in comparison with TiO_2 bulk ($E_g = 3.22$ eV). As shown in Fig. 8, with increasing the calcination temperature, the particle size increases and the absorption edge shows a red-shift (Table 1). This red shift suggests that band edge is size dependent. It is shown that the band gap of semiconductor nanocrystals decreases with an increase in their sizes and the absorption edge red-shifts, due to the quantum confinement effect [60].

It is well known that optical absorption of photocatalysts significantly influences their activity. Photoluminescence (PL) signals and their intensity are closely related to its photocatalytic activity [61]. PL spectra of the samples dried at 100°C are shown in Fig. 11. All the samples exhibit two considerable broad PL signals at 470 and 550 nm. The presence of these peaks in visible range is due to oxygen vacancies, defects, surface states, and other structural impurities [62–65]. An increase in concentration of oxygen vacancies can improve the photocatalytic activity [64]. In fact with increasing the concentration of oxygen vacancies as electron donors in TiO_{2-x} lattice, the amount of active absorbed oxygen species increases. Theoretically, because of the close radius of Fe^{3+} (0.064 nm) and Ti^{4+} (0.068 nm) ions, when Fe_2O_3 diffuses into TiO_2 lattice, Fe^{3+} will substitutes Ti^{4+} and create oxygen vacancies which results in more efficient photocatalytic activity [61–64]. The PL peaks intensities of 0.1 wt%- Fe_2O_3 - TiO_2 are larger than those of the other samples. Further addition of Fe_2O_3 content of the samples reduces the PL intensities, due to shorter distance of Fe–Fe ions, which result in an energy transfer between nearby ions. Therefore, a concentration quenching process will occur, due to a non-radiative decay process [63,64]. Fig. 12 also shows that by increasing the annealing temperature, the peaks intensities reduce, due possibly to the non-radiative transition shift to longer wavelengths and the PL peaks positions [63].

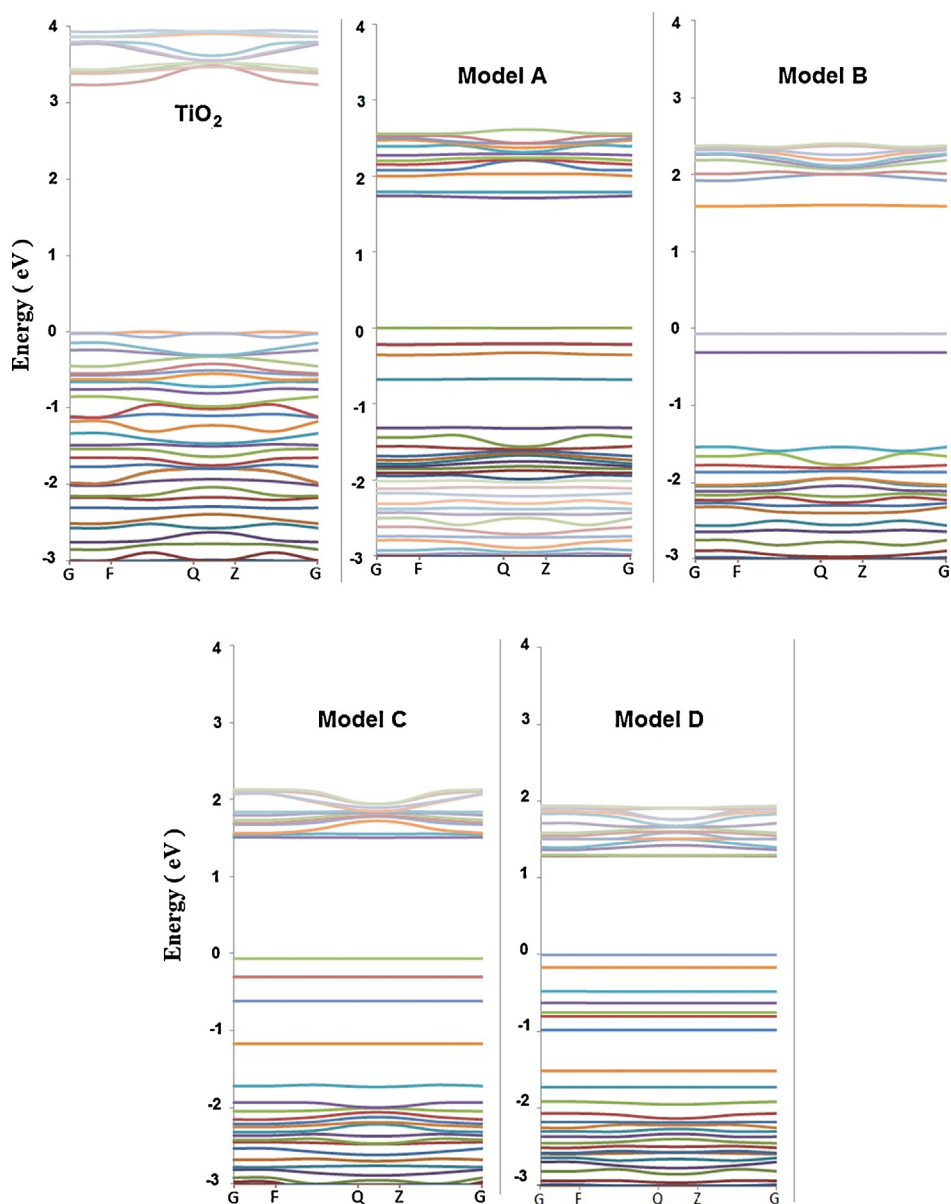


Fig. 9. Band structure plots of undoped TiO_2 , Fe^{3+} doped TiO_2 (Model A) FeO adsorbed on the anatase (1 0 1) surface (Model B), Fe_2O_3 adsorbed on the anatase (1 0 1) surface (Model C), and Fe_4O_6 cluster adsorbed on the anatase (1 0 1) surface (Model D).

3.2. Photocatalytic oxidation of trichloroethylene (TCE) in air

3.2.1. TCE photocatalytic oxidation products and degradation mechanism

Fig. 13 demonstrates the FTIR spectra of 500 ppm TCE in air as the feed (Fig. 13a) and the photocatalytic reactor effluent gases after 60 min time on stream (TOS), when 0.5 g of TiO_2 (Fig. 13b) or 0.1 wt% Fe_2O_3 – TiO_2 coated on the wire-mesh substrate are used (Fig. 13c). The FTIR spectrum of TCE in the feed (Fig. 13c) exhibits the peaks at 631 cm^{-1} and 783 cm^{-1} for C–Cl bending and 848 cm^{-1} for C–H bending vibrations. The spectra indicate broad bands around 3444 cm^{-1} ascribed to the vibration of O–H group, whereas the bands around 1631 cm^{-1} is assigned to the H–O–H bending of the water. CO_2 , CO and HCl appear in the FTIR at 2349 cm^{-1} and 2331 cm^{-1} for O=C=O bending vibrations, 2143 cm^{-1} for CO bending vibration, and at about 2900 cm^{-1} rotational bands for HCl [65–67]. There is no peak in the spectral features belonging to dichloroacetyl chloride (DCAC, CHCl_2COCl), phosgene (Cl_2CO) and trichloromethane (CHCl_3) [67]. Thus, the detected products from

TCE photooxidation are CO_2 , H_2O , HCl, and minor amounts of CO.

There have been several studies on the mechanism of the gas-phase photooxidation of TCE on TiO_2 . The previous studies [3,4,11,12,14,18,20,67,68,76] show that there are several different proposals for the mechanisms and reactive species of the photooxidation of TCE. Oxygen radical species created via UV activation of added O_2 are likely candidates to be primarily involved in attacking the TCE double bond in the initiation step (4). In another suggestion for radical initiated oxidative reaction path, TCE was degraded by OH radical species produced by the oxidation of water through photogenerated holes on the TiO_2 (5). One of the reaction products, Cl^- , is transformed to Cl radical species by direct oxidation on illuminated TiO_2 . These Cl radicals are reacted with the TCE, leading to the formation of undesirable chlorinated by-products (7). Nevertheless, the reaction mechanism and roles of O_2^- , OH and Cl radicals remained unclear.



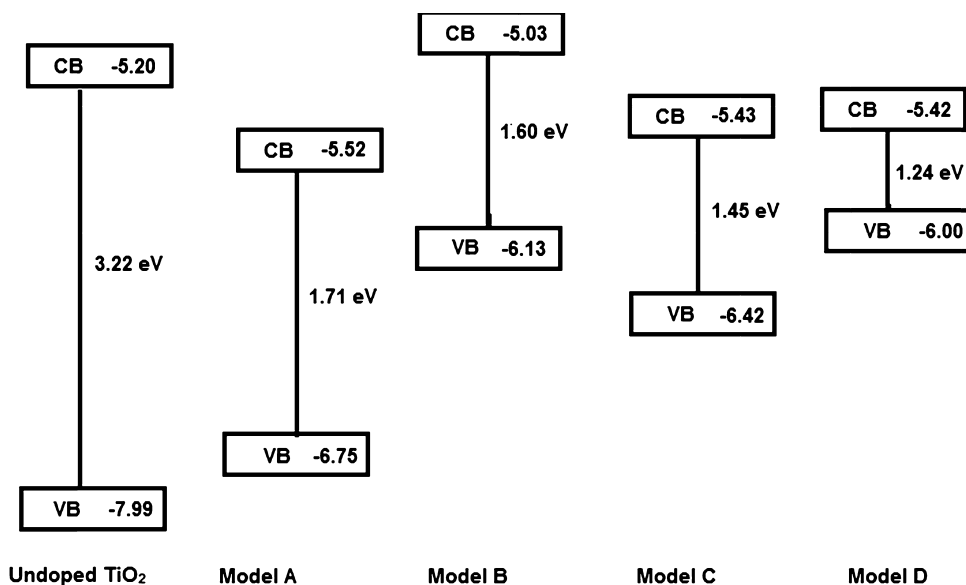
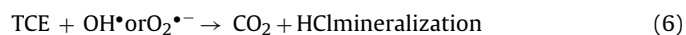


Fig. 10. Electronic structures of undoped TiO₂, Fe³⁺ doped TiO₂ (Model A) FeO adsorbed on the anatase (1 0 1) surface (Model B), Fe₂O₃ adsorbed on the anatase (1 0 1) surface (Model C), and Fe₄O₆ cluster adsorbed on the anatase (1 0 1) surface (Model D).



Based on the findings reported in references [3,12,67,68,76], the heterogeneous photocatalytic initiation, reactions (3)–(5), it is proposed that the initial step in the photooxidation is the excitation of adsorbed oxygen. The resultant holes can react with oxygen species to superoxide ($O_2^{\bullet-}$) radicals, which can sustain the mineralization process (6).

Based on our FTIR results, there are no organic reaction by-products from gas-phase photooxidation of TCE, in agreement with others results [4,6,8,9]. This may suggest that reductive reaction pathways would be more responsible for the decomposition of TCE, while interacting with the TiO₂ conduction band electrons (e^{-cb}) and anion superoxide radicals ($O_2^{\bullet-}$) [68].

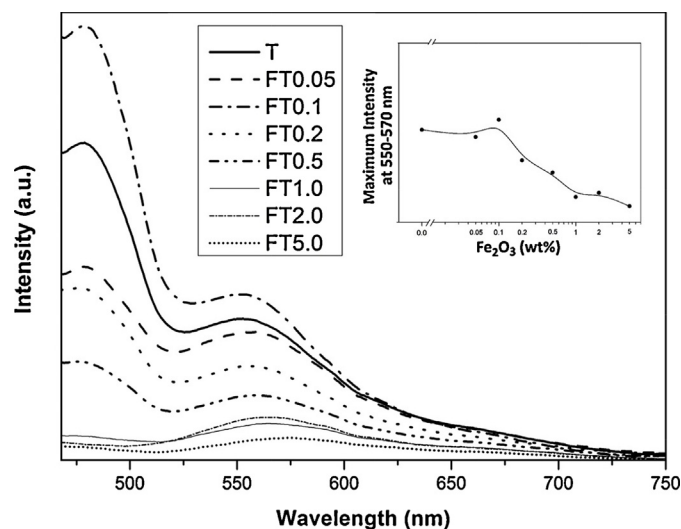


Fig. 11. The PL spectra of TiO₂ and 0.05–5.0% Fe₂O₃-doped TiO₂ samples. Inset: the maximum intensity (in 550–570 nm range) variation with the Fe₂O₃ content of the samples.

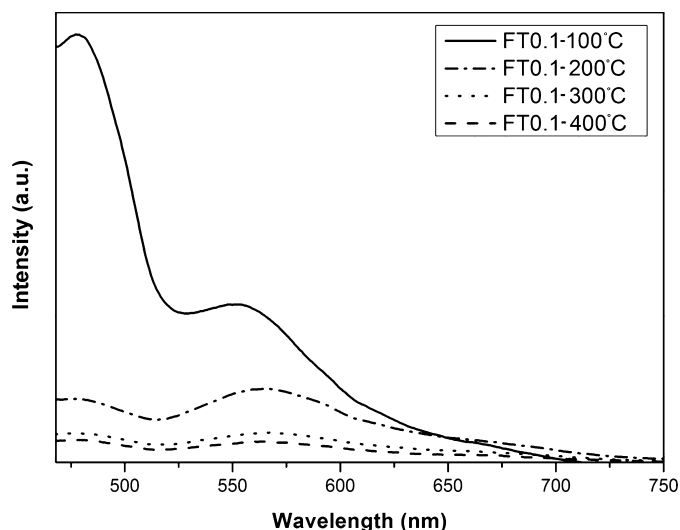


Fig. 12. The PL spectra of 0.1% Fe₂O₃-TiO₂ samples calcined at different temperatures.

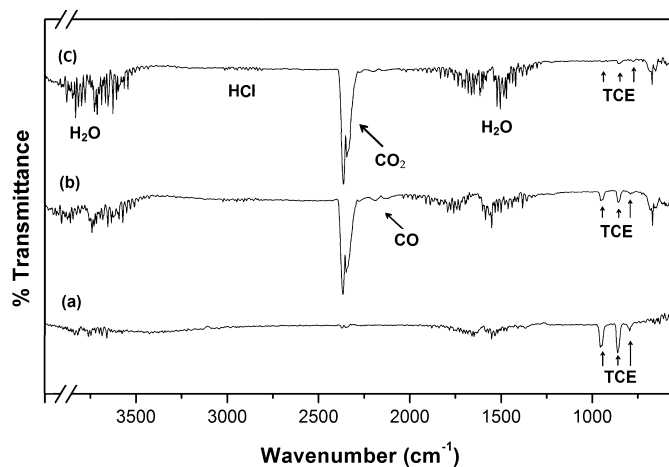


Fig. 13. FTIR spectra of (a) 500 ppm TCE in air as the feed (b) effluent gases from the photocatalytic reactor using 0.5 g TiO₂ coated on the substrate (c) the reactor effluent gases using 0.5 g FT0.1.

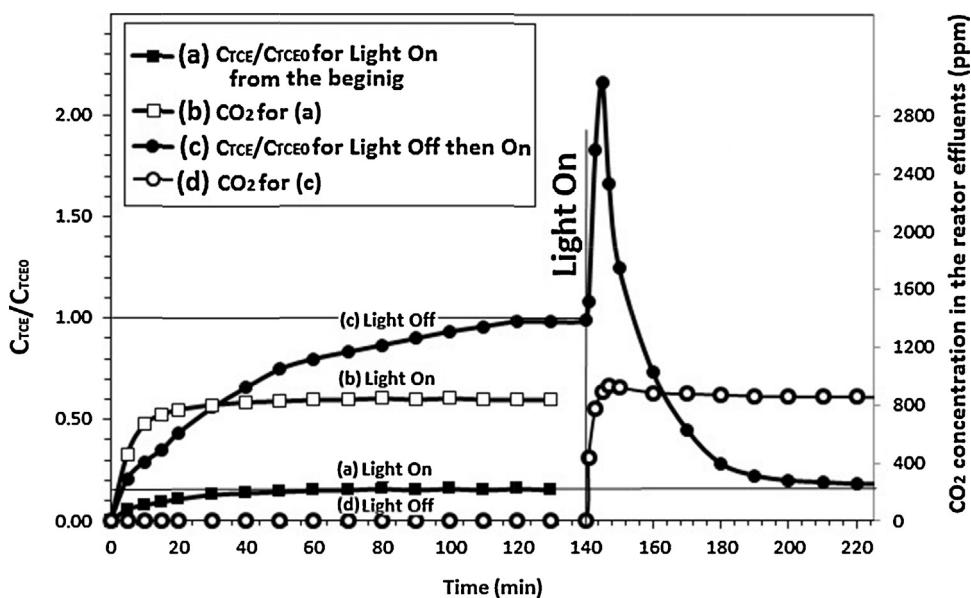


Fig. 14. Adsorption, desorption and degradation of TCE on 0.1% Fe_2O_3 - TiO_2 photocatalyst at two experimental conditions.

3.2.2. Adsorption of TCE on Fe_2O_3 -doped TiO_2 nanoparticles

Fig. 14 shows the adsorption, desorption and degradation of TCE on 0.5 g of 0.1 wt% Fe_2O_3 - TiO_2 photocatalyst coated on the substrate at two experimental conditions. First, from the beginning the UV lamp was switched on (Fig. 14a). The $C_{\text{TCE}}/C_{\text{TCE}0}$ ratio for this experimental conditions increases to a steady-state value of 0.15, corresponding to 85% conversion in about 50 min TOS. The smaller $C_{\text{TCE}}/C_{\text{TCE}0}$ ratio at shorter times can be ascribed to the adsorption of TCE on the photocatalyst, since during this time the CO_2 concentration increases to a steady-state value (Fig. 14b). Secondly, the UV lamp was switched off up to 140 min, when TCE effluent concentration reaches the stable concentration of the feed, and then the UV lamp was switched on for 80 more minutes (Fig. 14c). Under the light off period, no CO_2 as the TCE degradation products is detected (Fig. 14d) and TCE is accumulated by adsorption on the photocatalyst surface, until TCE saturates the surface after 140 min and the concentration of the reactor effluent reaches the feed concentration. When the light is switched on after 140, the TCE concentration in the effluents shows an overshoot and then decays to the same value of the $C_{\text{TCE}}/C_{\text{TCE}0}$ ratio as the first experiment (Fig. 14c). During this time, CO_2 concentration in the photocatalytic reactor effluents, after a minor overshoot, reaches the steady-state value, as that of the first experiment (Fig. 14d). However, $C_{\text{TCE}}/C_{\text{TCE}0}$ ratio shows a sharp and intense overshoot indicating that most of the TCE accumulated on the photocatalyst, by adsorption during the light off conditions, is desorbed.

3.2.3. Effects of Fe_2O_3 concentrations on photocatalytic activity of TiO_2

Fig. 15 shows the photocatalytic TCE oxidation on 0.5 g TiO_2 and the ones doped with various amounts of Fe_2O_3 dried at 100°C . TCE conversion on all the photocatalyst samples reach steady state values in about 50 min TOS. The runs repeated, after purging the photocatalysts with zero air for 30 min under UV irradiation, shows about the same values of TCE conversion variations with TOS. In accordance with Fig. 14, the TCE adsorption on the photocatalysts, but not their permanent deactivation, is the main source of decline in the TCE conversion with TOS. The strong adsorption of TCE on the photocatalysts usually results in a reversible deactivation [69].

Fig. 16 shows TCE degradation activities of 0.5 g and 1.0 g of photocatalysts containing various amounts of Fe_2O_3 , after

60 min TOS under UV irradiation. The photocatalysts containing 0.0–2.0 wt% Fe_2O_3 are significantly more active than P25. As the photocatalyst loading is doubled, the TCE conversion significantly increases. Among the photocatalysts, FT0.1 shows the highest photocatalytic activity of 85% and 97% degradation using 0.5 g and 1.0 g loadings of the photocatalysts, respectively. More than 0.1 wt% Fe_2O_3 addition to TiO_2 sharply suppresses the degradation activity of the photocatalysts. The photocatalytic activity of Fe-Ti mixed oxides for degradation of toxic compounds in water also has shown the same behavior of the maximum activity at an optimum concentration of iron oxide dopant [70–73].

FT0.1 with the highest photocatalytic activity for degradation of TCE shows the most intense PL peaks in the visible light region, indicating high vacancies in TiO_2 lattice in presence of Fe cations. These vacancies on the surface improve the adsorption of oxygen molecules, resulting in an increase in radicals' concentration. Furthermore, Fe cations can serve as mediators for interfacial charge transfer. This can enhance lifetime of electrons and holes due to

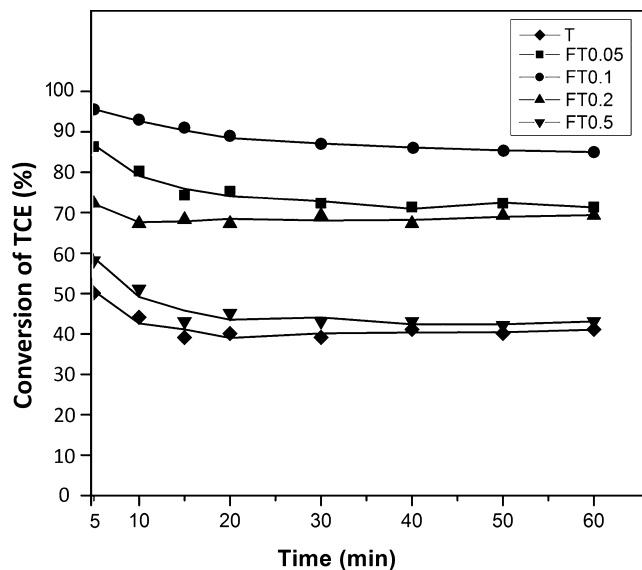


Fig. 15. Photocatalytic conversion of TCE on pure TiO_2 and 0.05–0.5% Fe_2O_3 - TiO_2 on 0.5 g photocatalyst under UV irradiation.

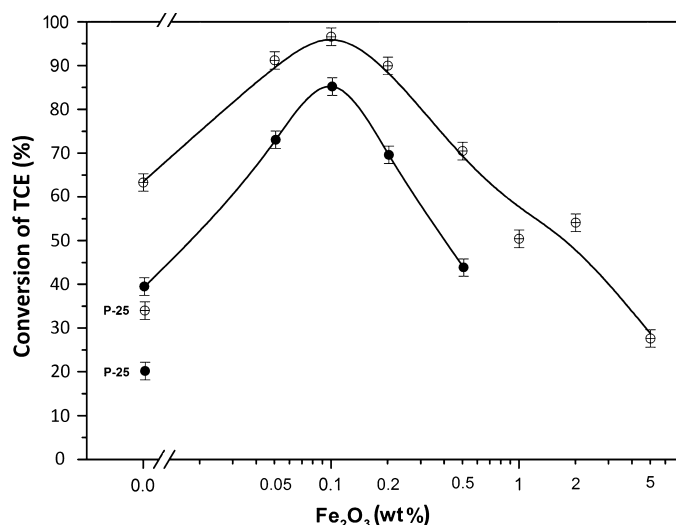


Fig. 16. Photocatalytic degradation of TCE on P-25, pure TiO₂ and 0.05–5.0% Fe₂O₃–TiO₂ samples after 60 min UV irradiation, using 1.0 g (⊕) and 0.5 g (●) photocatalyst.

electron/hole trapping at Fe centers. Moreover, the highest BET surface area of FT0.1 photocatalyst sample (Table 1) results in an enhanced TCE adsorption and hence photocatalytic activity. The concentration of vacancies, BET surface areas, and photocatalytic activities are lower for the samples containing less or more than 0.1 wt% Fe₂O₃. For more concentration of Fe₂O₃, the distance between trapping sites decreases and Fe₂O₃ can act as recombination centers through quantum tunneling. As a result, the recombination rate of the charge carriers increases and competes with the redox reactions on the surface of the photocatalyst, causing the photocatalytic activity to reduce [58,72–75]. Another important factor is trapping of the holes in Fe with less oxidizing power than the holes generated in TiO₂, resulting in the production of less thermodynamically favorable radicals [71]. It is reported that optimum Fe doping, high specific surface areas and small crystal sizes can enhance photocatalytic activity [53–57].

3.2.4. Effect of calcination temperature

The effects of Fe₂O₃-doped TiO₂ calcination temperature on the photocatalytic oxidation of TCE are shown in Fig. 17. Also the

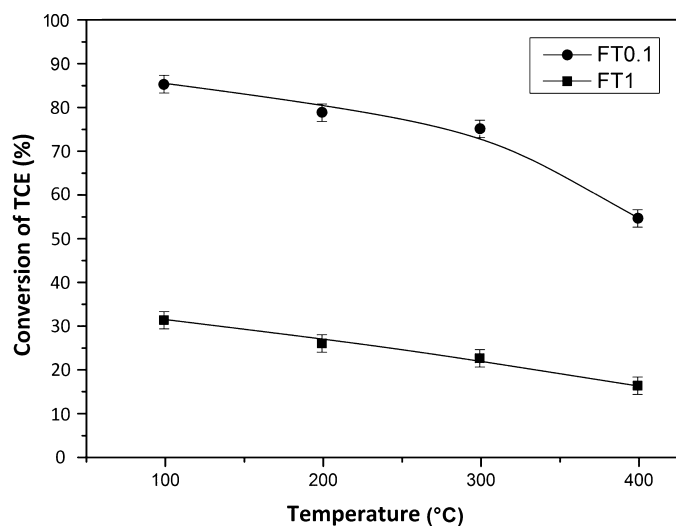


Fig. 17. Degradation of TCE on 0.5 g 0.1% Fe₂O₃–TiO₂ (FT0.1) and 1.0% Fe₂O₃–TiO₂ (FT1) calcined at different temperatures.

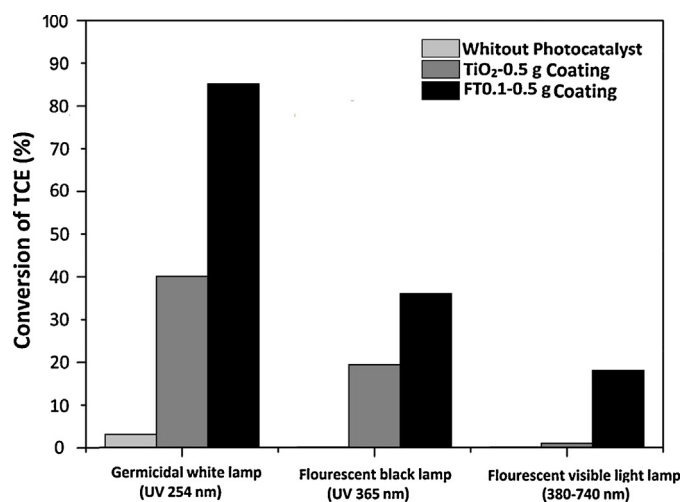


Fig. 18. TCE degradation without using photocatalyst and on the TiO₂ and FT0.1 photocatalysts, employing different lamps.

variation of some physical/chemical properties of FT0.1 sample with the calcination temperature is summarized in Table 1. No significant changes are observed in the band edges and their gaps, as the calcination temperature of FT0.1 increases. For both 0.5 g loadings of FT0.1 and FT1 containing 0.1 and 1.0 wt% Fe₂O₃, the TCE conversion significantly decreases, as the drying/calcination temperature increases from 100 to 400 °C (Fig. 17), while the BET surface areas decrease by a factor of 3.2 and crystallite sizes dramatically increase (Table 1). The average particle sizes obtained from BET surface area measurements are only slightly larger than those of the crystallite sizes. This indicates significant growth, rather than aggregation, of the crystallites. The dopants are isolated far from the surface and the transfer of the charge carriers to the surface is reduced, as the crystallite size increases [70].

3.2.5. Light wavelength and humidity effects and stability of the photocatalysts

The effect of light wavelength in UV and visible range on TCE degradation using 0.5 g of pure TiO₂, FT0.1 photocatalyst and without photocatalyst (blank test) after 60 min irradiation is shown in Fig. 18. 254 nm UV lamp (germicidal white), 365 nm UV lamp (fluorescent black) and visible fluorescent lamp (380–740 nm) were used as light sources all with 8W energy. No significant TCE degradation is found in the blank test with wire-mesh substrate containing no photocatalyst coating, expect 4% TCE photo-degradation for the germicidal white lamp.

On the synthesized TiO₂, considerable TCE photocatalytic conversion of 19% occurs under fluorescent black lamp irradiation, while the conversion under visible light irradiation is negligible. As 0.1 wt% Fe₂O₃ is doped into TiO₂, TCE conversion under the black lamp irradiation increases by about 1.9 times, while that under visible light irradiation dramatically enhances.

TCE has C–C, C–Cl, C=C, and C–H bonds with strengths of 82.6, 81.0, 145.8, 98.7 kcal mol^{−1}, respectively. The energy of these bonds can break by the germicidal white lamp (about 150 kcal mol^{−1}), while the energies of fluorescent black lamp (about 78 kcal mol^{−1}) and visible lamp (<72 kcal mol^{−1}) are not sufficient to break the bonds [76]. 254 nm UV light may produce more photons with energies in excess of the FT0.1 band gap of 3.02 eV [76]. Band gaps presented in Table 1 indicate that, under visible light irradiation, TiO₂ photocatalyst is not active, while FT0.1 photocatalyst is active.

Photocatalytic oxidation of TCE under visible light irradiation on the photocatalysts containing various contents of Fe₂O₃ is shown

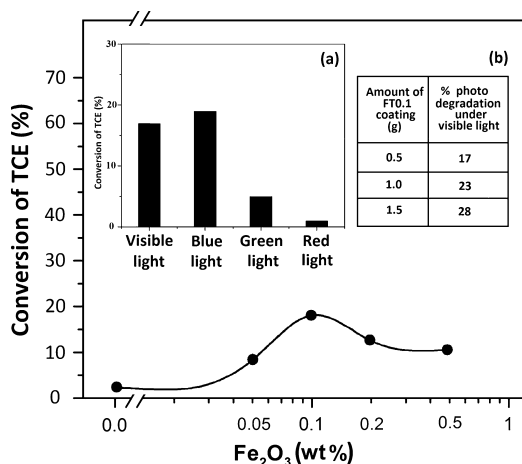


Fig. 19. Degradation of TCE under visible light irradiation on 0.05–0.5% Fe₂O₃-doped TiO₂ samples. Insets: (a) contribution of different portions of visible light to TCE degradation on 0.5 g FT0.1 and (b) the effect of the amounts of FT0.1 coating on the substrate on degradation of TCE under visible light irradiation.

in Fig. 19. The figure insets present the visible light degradation on FT0.1 using various loadings and visible light colors of blue, green and red with the same power of 8 W. Maximum TCE conversions are obtained on FT0.1 photocatalyst. The figure insets illustrate that the TCE photocatalytic conversion under visible light irradiation significantly increases with the FT0.1 photocatalysts loading and also the blue portion of the visible light mainly contributes to the photocatalytic TCE degradation.

As water vapor corresponding to 50% RH at room temperature is added to the zero air containing 500 ppm TCE, the TCE conversion does not change significantly. It is proposed that the adsorbed surface water in humid air is not involved in the TCE degradation [67,77].

The stability of 0.1 wt% Fe₂O₃-TiO₂ photocatalyst for the degradation of TCE under UV light irradiation is evaluated by repeating 60 min TOS runs (Fig. 20). Between two successive runs the photocatalyst was exposed to humid and dry zero air each for 30 min, both in the presence of UV light illumination. The six successive runs presented in Fig. 20 show no significant decline in the photocatalytic activity.

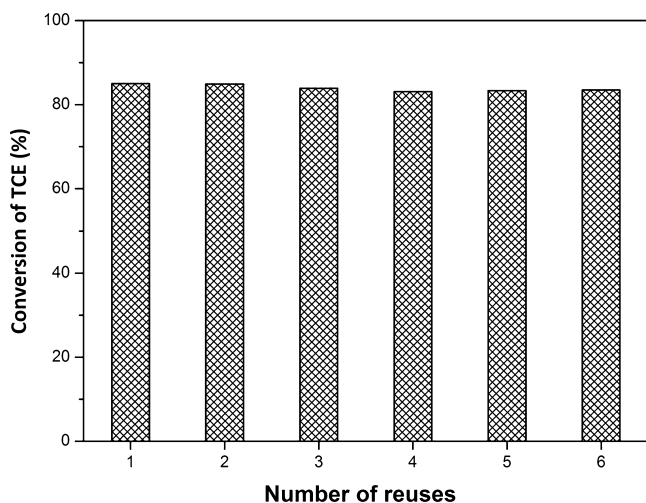


Fig. 20. Stability and durability of 0.1 wt% Fe₂O₃-TiO₂ photocatalyst for the degradation of TCE under UV light irradiation.

4. Conclusion

Fe₂O₃-doped TiO₂ photocatalysts were synthesized by an ultrasonic-assisted co-precipitation method and their activity on trichloroethylene (TCE) degradation under UV and visible light irradiations was investigated. All samples only dried at 100 °C show no XRD patterns, while HRTEM micrographs and Raman spectra show diffraction patterns for both hematite Fe₂O₃ and anatase TiO₂ and wide and weak peaks of anatase TiO₂ crystalline structures, respectively. In agreement with the experimental results, DFT predictions for four models of Fe₂O₃ doped into TiO₂ lattice and FeO and Fe₂O₃ and Fe₄O₆ cluster adsorbed on TiO₂ surface show that the band gaps reduce for all models. This leads to the visible light photoactivation of iron oxide-TiO₂.

The highest photocatalytic TCE conversion of 97% is observed for the FT0.1 sample containing 0.1 wt% Fe₂O₃ dried at 100 °C, with no calcination. FT0.1 sample exhibits the highest BET surface area and most intense PL peaks in the visible light region, which may enhance the TCE adsorption and surface defects, respectively. At relatively low concentrations, Fe³⁺ ions may incorporate into the TiO₂ lattice and serve as charge-transfer mediator with enhanced lifetimes of electrons and holes. At concentrations larger than 0.1 wt%, Fe₂O₃ may act as electron/hole recombination centers, rate of which competes with the redox reactions on the surface of the photocatalyst, resulting in the photocatalytic activity to reduce.

The band gaps of the Fe₂O₃-doped TiO₂ photocatalysts decrease, as Fe₂O₃ content of the samples increases. This leads to the photocatalytic oxidation of TCE in the visible light region. As the calcination temperature of FT0.1 increases, the BET surface area and PL peaks intensities in the visible region decrease, leading to suppressed photocatalytic activities. The Fe₂O₃-doped TiO₂ photocatalyst, just dried at 100 °C, with dramatically enhanced activity is a noteworthy choice for air purification.

Appendix A. Supplementary data

Supplementary data associated with this article can be found, in the online version, at <http://dx.doi.org/10.1016/j.apcatb.2014.10.023>.

References

- [1] J. Mo, Y. Zhang, Q. Xu, J. J. Lamson, R. Zhao, *Atmos. Environ.* 43 (2009) 2229–2246.
- [2] A.A. Firooz, A.R. Mahjoub, A.A. Khodadadi, M. Movahedi, *Chem. Eng. J.* 165 (2010) 735–739.
- [3] M.D. Driessen, A.L. Goodman, T.M. Miller, G.A. Zaharias, V.H. Grassian, *J. Phys. Chem. B* 102 (1998) 549–556.
- [4] M. Mohseni, *Chemosphere* 59 (2005) 335–342.
- [5] S. Maghsoodi, J. Towfighi, A.A. Khodadadi, Y. Mortazavi, *Chem. Eng. J.* 216 (2013) 827–837.
- [6] T.H. Lim, S.D. Kim, *Chemosphere* 54 (2004) 305–312.
- [7] S. Hager, R. Bauer, G. Kudiella, *Chemosphere* 41 (2000) 1219–1225.
- [8] L.A. Dibble, G.B. Raupp, *Catal. Lett.* 4 (1990) 345–365.
- [9] L.A. Dibble, G.B. Raupp, *Environ. Sci. Technol.* 26 (1992) 492–504.
- [10] S. Li, Q. Wang, T. Chen, Z. Zhou, Y. Wang, J. Fu, *Nanoscale Res. Lett.* 7 (1) (2012) 227–236.
- [11] M.R. Nimlos, W.A. Jacoby, D.M. Blake, T.A. Milne, *Environ. Sci. Technol.* 27 (1993) 732–740.
- [12] P.B. Amama, K. Itoh, M. Murabayashi, *J. Mol. Catal. A: Chem.* 217 (2004) 109–115.
- [13] M. Keshmiri, T. Troczynski, M. Mohseni, *J. Hazard. Mater. B* 218 (2006) 130–137.
- [14] P.B. Amama, K. Itoh, M. Murabayashi, *Appl. Catal. B* 37 (2002) 321–330.
- [15] J.Z. Kong, A.D. Li, X.Y. Li, H.F. Zhai, W.Q. Zhang, Y.P. Gong, H. Li, D. Wu, *J. Solid State Chem.* 183 (2010) 1359–1364.
- [16] M.D. Driessen, V.H. Grassian, *J. Phys. Chem. B* 102 (1998) 1418–1423.
- [17] S.E. Parka, H. Joob, J.W. Kang, *Sol. Energy Mater. Sol. Cells* 83 (2004) 39–53.
- [18] T. Tanimura, A. Yoshida, S. Yamazaki, *Appl. Catal. B* 61 (2005) 346–351.
- [19] H. Sun, R. Ullah, S. Chong, H.M. Ang, M.O. Tade, S. Wang, *Appl. Catal. B* 108 (2011) 127–133.
- [20] H.H. Ou, Sh.L. Lo, *J. Mol. Catal. A: Chem.* 275 (2007) 200–205.
- [21] B. Ohtani, Y. Ogawa, S.I. Nishimoto, *J. Phys. Chem. B* 101 (1997) 3746–3752.
- [22] C. Randorn, S. Wongnawa, P. Boonsin, *Sci. Asia* 30 (2004) 149–156.

- [23] M. Kanna, S. Wongnawa, P. Sherdshoopongse, P. Boonsin, *J. Sci. Technol.* 27 (2005) 1017–1026.
- [24] Z. Zhang, P.A. Maggard, *J. Photochem. Photobiol. A: Chem.* 186 (2007) 8–13.
- [25] J. Li, S. Liu, Y. He, J. Wang, *Microporous Mesoporous Mater.* 115 (2008) 416–425.
- [26] S. Buddde, S. Wongnawa, U. Sirimahachai, W. Puetpaibool, *Mater. Chem. Phys.* 126 (2011) 167–177.
- [27] E. Thimsen, S. Biswas, C.S. Lo, P. Biswas, *J. Phys. Chem. C* 113 (2009) 2014–2021.
- [28] C.C. Yen, D.Y. Wang, M.H. Shih, L.S. Chang, H.C. Shih, *Appl. Surf. Sci.* 256 (2010) 6865–6870.
- [29] J.P. Perdew, J.A. Chevary, S.H. Vosko, K.A. Jackson, M.R. Pederson, D.J. Singh, C. Fiolhais, *Phys. Rev. B* 46 (1992) 6671.
- [30] J. Yu, Q. Xiang, M. Zhou, *Appl. Catal. B* 90 (2009) 595–602.
- [31] Y. Yalçın, M. Kılıç, Z. Çınar, *Appl. Catal. B* 99 (2010) 469–477.
- [32] M. Nolan, *Phys. Chem. Chem. Phys.* 13 (2011) 18194–18199.
- [33] D.V. Wellia, Q.Ch. Xu, M.A. Sk, K.H. Lim, T.M. Lim, T.T.Y. Tana, *Appl. Catal. A* 401 (2011) 98–105.
- [34] M. Nolan, A. Iwaszuk, H. Tada, *Aust. J. Chem.* 65 (2012) 624–632.
- [35] K. Yang, Y. Dai, B. Huang, M.H. Whangbo, *Chem. Mater.* 20 (2008) 6528–6534.
- [36] K. Srinivas, K. Yesudas, K. Bhanuprakash, V.J. Rao, L. Giribabu, *J. Phys. Chem. C* 113 (2009) 20117–20126.
- [37] M. Kang, S.J. Choung, J.Y. Park, *Catal. Today* 87 (2003) 87–97.
- [38] S. Wongnawa, P. Boonsin, D. Kongkaew, S. Yodbutra, S. Pisuttanawat, *J. Trace Microprobe Technol.* 17 (1999) 25–37.
- [39] Z.L. Liu, Z.L. Cui, Z.K. Zhang, *Mater. Charact.* 54 (2005) 123.
- [40] X. Zhang, L. Lei, *Mater. Lett.* 62 (2008) 895–897.
- [41] Z. Yanqing, S. Erwel, C. Zhinzhan, L. Wenjun, H. Xingfang, *J. Mater. Chem.* 11 (2001) 1547–1551.
- [42] U. Arellano, J.A. Wang, M.T. Timko, L.F. Chen, S.P.P. Carrera, M. Asomoza, O.A.G. Vargas, M.E. Llanos, *Fuel* 126 (2014) 16–25.
- [43] X. Dong, J. Tao, Y. Li, H. Zhu, *Appl. Surf. Sci.* 256 (2010) 2532–2538.
- [44] T. Ohsaka, *J. Phys. Soc. Jpn.* 48 (1980) 1661.
- [45] S. Das, M.J. Hendry, *Chem. Geol.* 290 (2011) 101–108.
- [46] E. Smith, D. Geoffrey, *Modern Raman Spectroscopy: A Practical Approach*, Wiley, England, 2005, pp. 210.
- [47] H. Wang, J. Wei, R. Xiong, J. Shi, *J. Magn. Magn. Mater.* 324 (2012) 2057–2061.
- [48] M. Ivanda, S. Musić, S. Popović, M. Gotić, *J. Mol. Struct.* 480–481 (1999) 645–649.
- [49] J.W. Niemantsverdriet, *Spectroscopy in Catalysis*, Wiley, Netherlands, 2007, pp. 54.
- [50] A. Amarjargal, Zh. Jiang, L.D. Tijing, Ch.H. Park, I.T. Im, Ch.S. Kim, *J. Alloy Compd.* 580 (2013) 143–147.
- [51] W. Zhou, Ch. Cheng, J. Liu, Y.Y. Tay, J. Jiang, X. Jia, J. Zhang, H. Gong, H.H. Hng, T. Yu, H.J. Fan, *Adv. Funct. Mater.* 21 (2011) 2439–2445.
- [52] O. Carp, C.L. Huisman, A. Reller, *Prog. Solid State Chem.* 32 (2004) 33–177.
- [53] J. Zhu, W. Zheng, B. He, J. Zhang, M. Anpo, *J. Mol. Catal. A: Chem.* 216 (2004) 35–43.
- [54] M. Asiltürk, F. Sayllkan, E. Arpaç, *J. Photochem. Photobiol. A: Chem.* 203 (2009) 64–71.
- [55] C. Adán, A. Bahamonde, M. Fernández-García, A. Martínez-Arias, *Appl. Catal. B* 72 (2007) 11–17.
- [56] K. Esquivel, R. Nava, A.Z. Méndez, M.V. González, O.E.J. Acunad, L.E. Alarcón, J.M.P. Hernández, B. Pawelec, J.L.G. Fierro, *Appl. Catal. B* 140 (2013) 213–224.
- [57] S. Song, B. Jun, G. Chen, D. Jianjun, *Rare Met.* 30 (2011) 147–152.
- [58] L. Cui, F. Huang, M. Niu, L. Zeng, J. Xu, Y. Wang, *J. Mol. Catal. A: Chem.* 326 (2010) 1–7.
- [59] W. Zhang, Y. Chen, Sh. Yu, Sh. Chen, Y. Yin, *Thin Solid Films* 516 (2008) 4690–4694.
- [60] H. Zhu, D. Yang, G. Yu, H. Zhang, K. Yao, *Nanotechnology* 17 (2006) 2386–2389.
- [61] D. Li, H. Haneda, S. Hishita, N. Ohashi, *Chem. Mater.* 17 (2005) 2596–2602.
- [62] J. Zhang, Y. Hu, M. Matsuoka, H. Yamashita, M. Minagawa, H. Hidaka, M. Anpo, *J. Phys. Chem. B* 105 (2001) 8395–8398.
- [63] N. Nasralla, M. Yeganeh, Y. Astuti, S. Piticharoenphun, N. Shahtahmasebi, A. Kompany, M. Karimipour, B.G. Mendis, N.R.J. Pootlon, L. Šiller, *Sci. Iran.* 20 (2013) 1018–1022.
- [64] J. Liqiang, Q. Yichun, W. Baiqi, L. Shudan, J. Baojiang, Y. Libin, F. Wei, F. Honggang, S. Jiazhong, *Sol. Energy Mater. Sol. Cells* 90 (2006) 1773–1787.
- [65] A.A. Telke, S.M. Joshi, S.U. Jadhav, D.P. Tamboli, S.P. Govindwar, *Biodegradation* 21 (2010) 283–296.
- [66] J.C.S. Wu, C.H. Chen, *J. Photochem. Photobiol. A: Chem.* 163 (2004) 509–515.
- [67] J. Fan, J.T. Yates, *J. Am. Chem. Soc.* 118 (1996) 4686–4692.
- [68] N. Wu, J. Wang, D.N. Tafen, H. Wang, J.G. Zheng, J.P. Lewis, X. Liu, S.S. Leonard, A. Manivannan, *J. Am. Chem. Soc.* 132 (2010) 6679–6685.
- [69] E. Piera, J.A. Ayllón, X. Doménech, J. Peral, *Catal. Today* 76 (2002) 259–270.
- [70] J.A. Navío, G. Colón, M.I. Litter, G.N. Bianco, *J. Mol. Catal. A: Chem.* 106 (1996) 267–276.
- [71] M.I. Litter, J.A. Navío, *J. Photochem. Photobiol. A: Chem.* 84 (1994) 183–193.
- [72] Libera, J. Elam, N. Sather, T. Rajh, N.M. Dimitrijevic, *Chem. Mater.* 22 (2010) 409.
- [73] (a) H. Tada, Q. Jin, H. Nishijima, H. Yamamoto, M. Fujishima, S.i. Okuoka, T. Hattori, Y. Sumida, H. Kobayashi, *Angew. Chem. Int. Ed.* 50 (2011) 3501–3505; (b) Q. Jin, M. Fujishima, H. Tada, *J. Phys. Chem. C* 115 (2011) 6478–6483.
- [74] J.A. Navío, G. Colon, M. Macias, C. Real, M.I. Litter, *Appl. Catal. A* 177 (1999) 111–120.
- [75] T. Umebayashi, T. Yamaki, H. Itoh, K. Asai, *J. Phys. Chem. Solids* 63 (2002) 1909–1920.
- [76] Y. Ku, Ch.M. Ma, Y.Sh. Shen, *Appl. Catal. B* 34 (2001) 181–190.
- [77] H.H. Ou, Sh.L. Lo, *J. Hazard. Mater.* 146 (2007) 302–308.